Journal of Power Sources 195 (2010) 5726–5730

Contents lists available at ScienceDirect

Journal of Power Sources

journal homepage: www.elsevier.com/locate/jpowsour

Short communication

Statistical continuum mechanics analysis of effective elastic properties in solid oxide fuel cell glass–ceramic seal material

J. Milhans[a,*], D. Li[a], M. Khaleel[b], X. Sun[b], H. Garmestani[a]

[a] School of Material Science and Engineering, Georgia Institute of Technology, Atlanta, GA 30332-0245, United States
[b] Fundamental and Computational Sciences Directorate, Pacific Northwest National Laboratory, Richland, WA 99354, United States

ARTICLE INFO

Article history:
Received 8 March 2010
Received in revised form 24 March 2010
Accepted 25 March 2010
Available online 31 March 2010

Keywords:
Solid oxide fuel cell
Glass–ceramic
Two-point correlation function
Temperature dependent modulus
Aging

ABSTRACT

A full statistical analysis of the microstructure of glass–ceramic solid oxide fuel cell (SOFC) seal material, G18, is performed to calculate elastic properties. Predictions are made for samples aged for 4 h and 1000 h, giving different crystallinity levels. Microstructure of the glass–ceramic G18 is characterized by correlation function for each individual phase. Predicted results are compared with the Voigt and Reuss bounds in this study. The weak contrast analysis results in elastic modulus predictions between the upper and lower bounds but closer to the upper bound.

1. Introduction

1.1. Background

SOFCs have a promising future as an alternative power source. SOFCs are quiet, fuel flexible (hydrogen or carbon monoxide), efficient, and have size flexibility. Among all the SOFC designs, planar SOFCs have by far the highest power density. One of the main challenges in the development of planar SOFC is that they require a hermetic seal between the fuel and air sides of the electrodes. Seals may also be used to connect the components within the fuel cell. Glass–ceramic SOFC seals are usually made by tape casting green tape and sintered.

The main seal functions include preventing mixing of oxidants and fuel, preventing leaking of oxidants and fuel, electrically isolating cells from each other, and serving as a bond between components. If the seal allows mixing or leaking of the fuel and oxidants, the performance of the SOFC will degrade significantly, and may not even function. Also, because the seal is bonded to the components in the fuel cell, such as the cathode, electrolyte, and anode, the seal must be functional for the entire design lifetime of the fuel cell [1–3].

In order to increase fuel cell life and cut costs of seal optimization, it is necessary to investigate the relationship between the microstructure and material properties. This seal must be stable under thermal cycling, chemically compatible and structurally strong. The seal should also have mechanical and thermal properties that are similar to the neighboring components within the cell. The main property that needs to be matched is the coefficient of thermal expansion. For most ceramic fuel cell components, such as the anode, cathode, and electrolyte, this is a CTE of about $10–11 \times 10^{-6}\,K^{-1}$, and $12 \times 10^{-6}\,K^{-1}$ for the metal interconnects [1,4–6]. In general, it is desired to more closely match the CTE of the ceramic materials, as they are more prone to cracking and damage. Thermally induced stress is a very important issue in predicting fuel cell life during thermal cycling. In order to predict thermal induced stress, elastic properties must be investigated.

In this study, statistical two-point correlation functions have been calculated from SEM images of aged and unaged G18 with different crystallinity. Using two-point correlation functions is a numerically efficient methodology to characterize microstructures and extract information about volume fractions and the details of the microstructure such as morphology, clustering or banding [7–13]. These correlation functions can be used to represent the entire microstructure if the microstructure is uniform in all three dimensions, which is the case of the material in this study. These two-point correlations will be used in a homogenization scheme to predict the elastic modulus of the seal material.

* Corresponding author at: Georgia Institute of Technology, 771 Ferst Dr., Love Bldg Rm 353, Atlanta, GA 30332, United States. Tel.: +1 978 870 7944; fax: +1 404 894 9140.
E-mail address: jackie.milhans@gmail.com (J. Milhans).

0378-7753/$ – see front matter © 2010 Elsevier B.V. All rights reserved.
doi:10.1016/j.jpowsour.2010.03.079

1.2. Material

Glass–ceramic seals have been commonly used in solid oxide fuel cells (SOFCs) due to their low cost and ease of manufacturing. Glass–ceramics are resistant to degradation and are excellent for high temperature applications. They are good candidates for hermetic seals, since SOFCs operate at high temperatures, usually between 700 °C and 1000 °C. On the other hand, these glass–ceramic seals can also be vulnerable to damage and failure, due to their brittle nature, unwanted chemical reactions, or porosity. The reliability of the seal is of paramount importance, since it separates the multiple chambers of the fuel cell and prevents reactants and products from mixing. If the seal is not chemically compatible or susceptible to degradation, this can lead to a waste of fuel and can pose as a safety hazard [3,14]. Replacing failed seal is very time consuming and costly, since it is inside of the fuel cell and bonded to several parts of the cell. Development of a dependable, durable seal prolongs the life of the fuel cell. Therefore it is a critical element in SOFC commercialization.

The Pacific Northwest National Laboratory (PNNL) has developed a glass–ceramic, i.e. G18 for potential application in SOFCs. G18 is a barium–calcium–aluminosilicate (BCAS)-based glass, with boron oxide added for better control over the coefficient of thermal expansion and viscosity. After the initial sintering of the glass, a crystallization of approximately 55% barium silicate has been observed. There are also small amounts of other phases, including hexacelsian ($BaAl_2Si_2O_8$ with a hexagonal structure) crystalline phase and an unknown solid solution amorphous phase. The rest of the material stays as glassy phase. This glass–ceramic has shown increasing crystallization, up to 72%, after aging and thermal cycling. Unfortunately, at the same time, the hexacelsian develops a monoclinic structure, causing the coefficient of thermal expansion (CTE) to decrease. This low CTE leads to cracking in the seal, because the seal cannot expand with the rest of the materials in the cell. That is to say, when the fuel cell is heated after thermal cycling, the sealant remains attached to the neighboring materials, but cracks are initiated and grow since the sealant cannot expand at the same rate [1,4,14–17].

The G18 samples shown in Figs. 1–4 are sintered in air at 850 °C for an hour, and then aged for 4 h at 750 °C. Further aging is then done at 750 °C for samples aged for 1000 h. For the images of the samples that had been heated to 800 °C, it is assumed that the microstructure did not heavily change in morphology of volume fraction after being cooled to take the SEM image, and therefore can compare high temperature elastic property data to prediction results. These samples had been heated to 800 °C for four-point flexural tests in another study. The images show that there was some change to the microstructure due heating and cooling.

As previously mentioned, crystallinity in the initial sintering of the G18 is around 55%. The main crystallized phase is barium silicate, which appears as the white phases in Figs. 1–4, in the amorphous phase, showing as the grey phase. With further aging, small

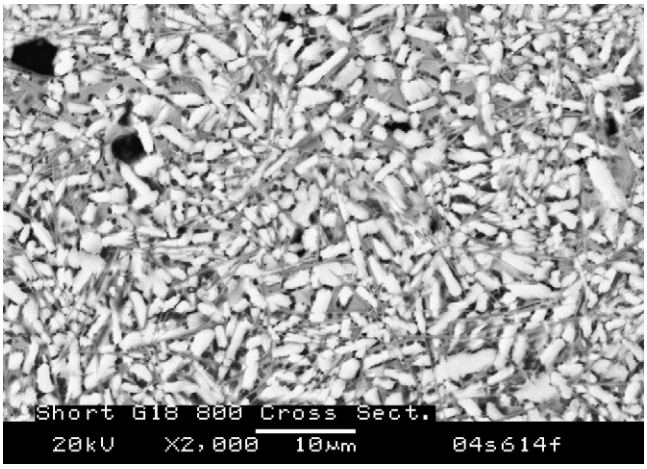

Fig. 2. G18 aged for 4 h and heated again to 800 °C and cooled.

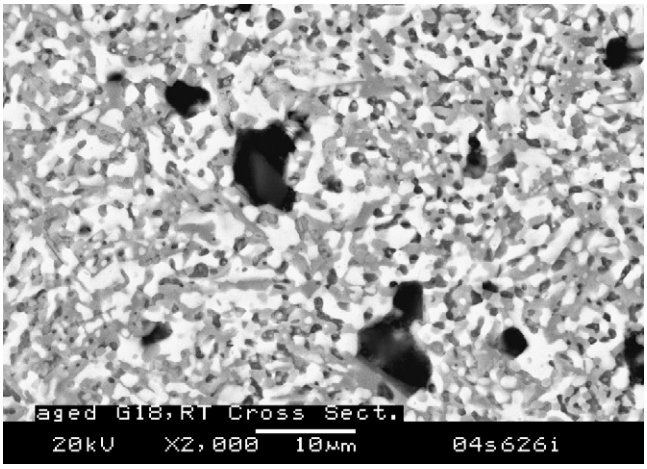

Fig. 3. G18 aged for 1000 h.

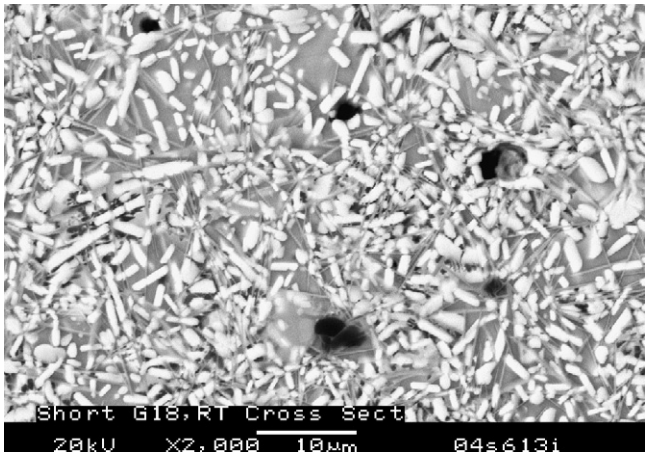

Fig. 1. G18 aged for 4 h.

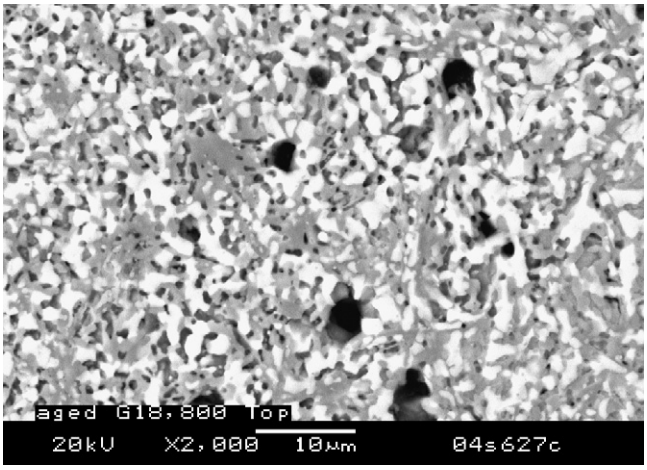

Fig. 4. G18 aged for 1000 h and heated again to 800 °C and cooled.

Table 1
Elastic and shear modulus of unaged and aged G18 at different temperatures [7,24,25].

Sample	Elastic modulus (GPa)	Shear modulus (GPa)
G18 aged 4 h (22 °C)	77.7	30.5
G18 aged 4 h (600 °C)	67.7	26.4
G18 aged 1000 h (22 °C)	60.8	25.7
G18 aged 1000 h (800 °C)	67.4	27.5

amounts of other phases form in the glassy matrix, including hexacelsian (hexagonal $BaAl_2Si_2O_8$), monoclinic celsian ($BaAl_2Si_2O_8$), and $(Ba_xCa_y)Si_4$. The hexacelsian, which appear as the darker grey, sharp needles in Figs. 1 and 2, is not clearly shown in Figs. 3 and 4, leaving only slight outlines of the phase. The darkest phase in the micrographs are pores, which are much smaller and surround the barium silicate phase in the 1000 h aged samples. The unknown crystalline phases and monoclinic celsian are not seen in these images.

After the initial heat treatment, barium silicate appears as needle-like phase. These needles have grown with no preference to orientation. With further aging, darker needles of hexacelsian begin to appear. These needles are shorter and smaller, while they are still much less significant in volume fraction when compared with barium silicate and glassy phases [1].

The elastic and shear modulus values of G18 are given in Table 1 [6,18,19].

2. Effective property predictions

2.1. Two-point correlation functions

Two-point correlation functions are used in a statistical homogenization framework to characterize different types of heterogeneous media. They are useful in the sense that they can contain descriptive information about the microstructure being studied, including volume fraction, clustering, and spacing of phases [9,10,20,21]. Vectors with given orientation and length are drawn onto the image at random position. As the system is a two-phase composite, the phases at the endpoints are either phase 1 (barium silicate) or phase 2 (amorphous). In this study, the minor phases are included in the amorphous phase. This is because of the closeness in elastic properties of hexacelsian and silica [22], and also, monoclinic celsian and other solid solutions are not observed. Two-point correlation function is a probability function, P_{ij}, where i is the phase of the initial point, and j is the phase at the end of the vector. These operations result in four different variables, P_{11}, P_{12}, P_{21}, and P_{22}, satisfying the normality conditions, where ν_i is the volume fraction of phase i:

$$P_{11} + P_{12} = \nu_1 \tag{1}$$

$$P_{21} + P_{22} = \nu_2 \tag{2}$$

$$P_{12} = P_{21} \tag{3}$$

As a result, only one of these probabilities is an independent variable. Several analytical formulations have been proposed to represent correlation statistics that can satisfy the above conditions. The most popular one was postulated by Corson [23,24] in 1976 as an exponential regression function to represent two-point probability functions for an isotropic two-phase random media:

$$p_{ij}(\vec{r}) \equiv \nu_i\nu_j + (-1)^{i+j}\nu_i\nu_j \ \exp(-c_{ij}r^{n_{ij}}) \tag{4}$$

Here, c_{ij} and n_{ij} are empirical constants determined by a least square error curve fit to the experimental data.

2.2. Effective elastic modulus

Starting from the elastic properties of each component of the two-phase composite and microstructure represented by correlation functions, the effective properties will be predicted by statistical continuum model described below. Here, effective stiffness tensor is defined as **C**, local stiffness tensor at location r as $c(r)$. Ergodicity condition is assumed here for the statistical framework. The ensemble average, over the representative volume, V, will be denoted using brackets $\langle\rangle$. The average elastic moduli is then [25,26]:

$$\left\langle c_{ijkl}\right\rangle = \left\langle c_{ijkl}(r)\right\rangle = \frac{1}{V}\int_V c_{ijkl}(r)\,dV \tag{5}$$

Using Hill's condition and making the assumption of Kröner for an infinite medium, the stiffness tensor can be written as (for details, see Refs. [8,9]):

$$\langle\boldsymbol{\varepsilon}\boldsymbol{\sigma}\rangle = \langle\boldsymbol{\varepsilon}\mathbf{c}\boldsymbol{\varepsilon}\rangle = \langle\boldsymbol{\varepsilon}\rangle\,\langle\mathbf{c}\boldsymbol{\varepsilon}\,\rangle \tag{6}$$

where $\boldsymbol{\varepsilon}$ is the local strain tensor and **c** is the local stiffness tensor. This can be used to define **C**:

$$\langle\boldsymbol{\varepsilon}\rangle\mathbf{C}\langle\boldsymbol{\varepsilon}\rangle = \langle\boldsymbol{\varepsilon}\mathrm{C}\boldsymbol{\varepsilon}\rangle, \text{ therefore, } \mathbf{C}\langle\boldsymbol{\varepsilon}\rangle = \langle\mathbf{c}\boldsymbol{\varepsilon}\,\rangle \tag{7}$$

If $\boldsymbol{\sigma}$ and $\boldsymbol{\varepsilon}$ are ergodic, then one can write:

$$\boldsymbol{\varepsilon} = \langle\boldsymbol{\varepsilon}\rangle + \boldsymbol{\varepsilon}'; \boldsymbol{\sigma} = \langle\boldsymbol{\sigma}\rangle + \boldsymbol{\sigma}'; \mathbf{c} = \langle\mathbf{c}\rangle + \mathbf{c}' \tag{8}$$

where the $'$ denotes the local deviation from the average and $\langle\boldsymbol{\sigma}'\rangle = \langle\boldsymbol{\varepsilon}'\rangle = \langle\mathbf{c}'\rangle = 0$. To represent local inhomogeneity, a fourth rank tensor is defined, **a**, such that:

$$\mathbf{C} = \langle\mathbf{c}\rangle + \left\langle\mathbf{c}'\mathbf{a}\right\rangle \tag{9}$$

After solving for **a**, which can be seen in depth in the work by Lin and Garmestani [8], using above equations and denoting the stiffness for the two phases as $c1$ and $c2$, respectively, we are left with:

$$C_{abmn} = \left\langle c_{abmn}\right\rangle - \int_V drG_{ik,jl}(r)\{c1'_{abkl}c1'_{ijmn}P_{11} + c1'_{abkl}c2'_{ijmn}P_{12} + c2'_{abkl}c1'_{ijmn}P_{21} + c2'_{abkl}c2'_{ijmn}P_{22}\} \tag{10}$$

or in short form:

$$\mathbf{C} = \langle\mathbf{c}\rangle = G \times \mathbf{F}$$

where **F** is an 8th rank tensor:

$$\mathbf{F}_{abklijmn} = c1'_{abkl}c1'_{ijmn}P_{11} + c1'_{abkl}c2'_{ijmn}P_{12} + c2'_{abkl}c1'_{ijmn}P_{21} + c2'_{abkl}c2'_{ijmn}P_{12} \tag{11}$$

G is the Green's function, defined as the Fourier integral over k-space:

$$G_{lm}(r) = \frac{1}{8\pi^3}\int_{k\in k^3}\tilde{G}_{lm}(k)e^{ikr}dk^3 = \frac{1}{8\pi\bar{\mu}|r|}\left\{2\delta_{lm} - \frac{\bar{\lambda}+\bar{\mu}}{\bar{\lambda}+2\bar{\mu}}\left(\delta_{lm} - \frac{r_l r_m}{|r|^2}\right)\right\} \tag{12}$$

with the vector, $\mathbf{r} = r_2 - r_1$ (r_i denoting the endpoints of the vector **r** in the microstructure), δ is the Dirac delta function, and μ and λ are Lamé constants for isotropic tensor $\langle\mathbf{c}\rangle$, where the bar indicates that they are averaged. Further details can be seen in Refs. [8,27].

2.3. Voigt and Reuss bounds

The Voigt [28] upper bound and Reuss [29] lower bound are well-known bounds, used here to validate homogenization

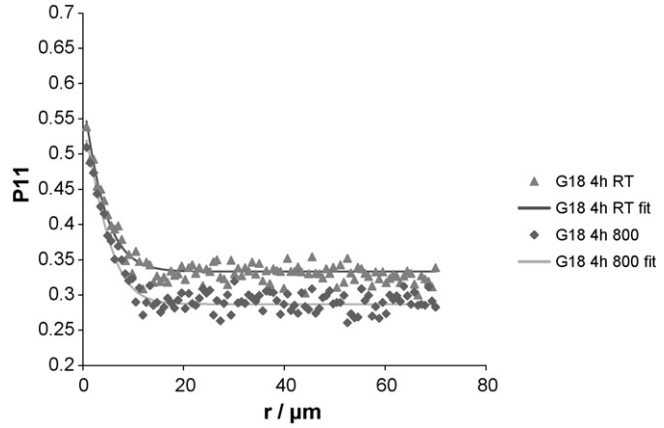

Fig. 5. Two-point correlation functions and fitted curves for samples not reheated.

methodology used here. The Voigt bound may be considered as predicting the elastic constants of the composite with inclusion and matrix phases arranged in parallel, or assuming a uniform strain field. On the other hand, the Reuss bound takes inclusion and matrix phases arranged in series resulting in a uniform stress field. In the two bounds, the microstructures are simply characterized by volume fractions of components. These two bounds generally deviate from each other, especially when the crystalline volume fraction is quite high or if there is a large difference in individual phase property values. The effective stiffness tensor, **C**, for the Voigt and Reuss bounds can be calculated as below:

$$\mathbf{C}_{\text{Voigt}} = \langle \mathbf{C} \rangle \tag{13}$$

$$\mathbf{C}_{\text{Reuss}} = \langle \mathbf{C}^{-1} \rangle^{-1} \tag{14}$$

3. Results

Microstructures shown in Figs. 1–4 are characterized using two-point correlation functions. Analytical curves proposed by Corson were then fitted to the correlation functions.

Figs. 5 and 6 give the experimental two-point correlation functions and the simulated correlation functions represented by the exponential regression function of images of samples after initial heat treatments and samples which were heated to 800 °C and cooled, respectively. Error from fitting the experimental two-point function data to Corson's function is demonstrated in Table 2. With Chi-squared errors much less than 5%, the exponential regression

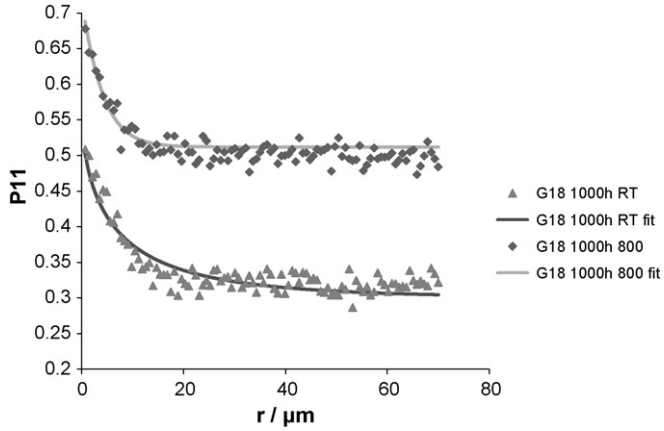

Fig. 6. Two-point correlation functions and fitted curves for samples heated again to 800 °C and cooled.

Table 2
Curve fitting accuracies.

Sample	Chi-squared	Adjusted R^2
G18 4 h aged (RT)	1.56E−04	0.90139
G18 4 h aged (800 °C)	2.06E−04	0.89957
G18 1000 h aged (RT)	2.85E−04	0.84401
G18 1000 h aged (800 °C)	2.31E−04	0.81438

Table 3
Elastic properties of individual phases [30–32].

Material	Young's modulus (GPa)	Shear modulus (GPa)
Barium silicate	69.0	28.3
Silica glass (25 °C)	73.0	31.5
Silica glass (800 °C)	80.0	33.0

function is a good analytical formula to describe two-point function.

Properties of individual components of the two-phase composite are shown in Table 3 [30–32]. Barium silicate has the same elastic modulus at both 25 °C and 800 °C [33]. Volume fractions of crystalline and amorphous phases in each microstructure are given in Table 4. Properties of silica glass were used to estimate the properties of the matrix phase, due to the high glass transition temperature, similar behavior in increasing modulus with respect to increasing temperature in 1000 h aged G18, and similar chemical compositions.

Because there is no strong contrast in crystalline and amorphous phases, the Voigt–Reuss bounds are very close. The Voigt and Reuss bounds, classical upper and lower bounds are given by the following equations for composites of N phases:

$$E_V = \sum_{i=1}^{N} E_i \phi_i \tag{15}$$

$$\frac{1}{E_R} = \sum_{i=1}^{N} \frac{\phi_i}{E_i} \tag{16}$$

where E denotes elastic property (Young's modulus or shear modulus), ϕ volume fraction, and i phase identity.

Figs. 7 and 8 show the effective property predicted by statistical continuum mechanics model, the Voigt and Reuss bounds for the Young's modulus and shear modulus, respectively. From the microstructures in Figs. 1–4, the two-point correlation function prediction of the effective Young's modulus and shear modulus falls within Voigt bound and Reuss bound, while being closer to the Voigt upper bound. The predicted properties do not match the exact properties of G18, shown in Table 1, since the properties of the actual individual phases were not used in this calculation, due to unavailability of data. The model using two-point correlation functions is accurate in its prediction of G18, using the properties for individual phases shown in Table 3. This is because both the shear and elastic modulus predictions fall within the Voigt and Reuss bounds. Possible error may be due to porosity affecting the volume fractions and exponential regression curve fitting error. It is promising that this method can be used, due to the comparable data used, results, and the properties of G18.

Table 4
Volume fractions of phases for Figs. 1–4.

Sample	Crystalline	Amorphous
G18 4 h aged (RT)	0.53	0.47
G18 4 h aged (800 °C)	0.54	0.46
G18 1000 h aged (RT)	0.55	0.45
G18 1000 h aged (800 °C)	0.72	0.28

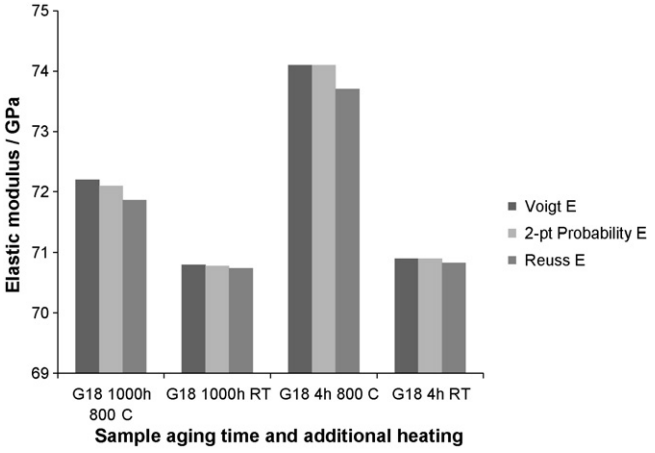

Fig. 7. Effective Young's modulus predictions.

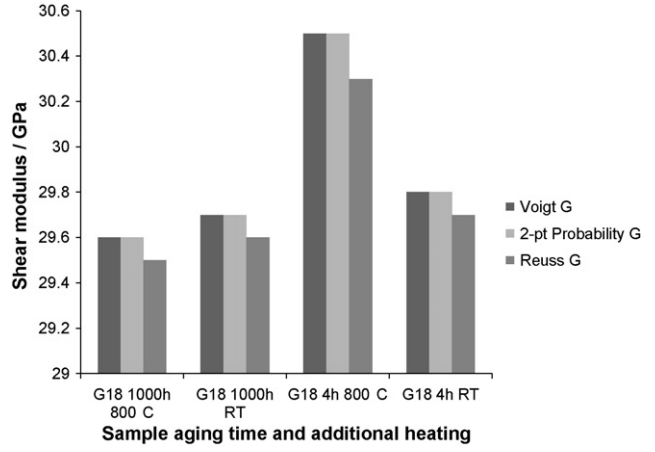

Fig. 8. Effective shear modulus predictions.

4. Conclusions

Two-point correlation functions have been used to characterize the microstructures of random, uniform glass–ceramic seal materials with different aging temperatures and durations. A simple exponential regression function was used to represent the two-point correlation function. Elastic properties are predicted from the microstructure represented by two-point function and individual properties by statistical continuum mechanics. Predicted results falls within the Voigt and Reuss bounds. The weak contrast in individual elastic property values may account for effective moduli calculated to be closer to Voigt bound. The two-point correlation function method has shown that it is, in general, a reasonable method to find the effective modulus for these types of BCAS-based glass–ceramics. More importantly, the two-point correlation function method maybe further used to optimize the volume fraction and morphology of the ceramic phase to engineer the elastic modulus of the SOFC seal to ensure its structural integrity during operation and thermal cycling.

Acknowledgements

The Pacific Northwest National Laboratory is operated by Battelle Memorial Institute for the United States Department of Energy under Contract DE-AC06-76RL01830. The work summarized in this report was funded as part of the Solid-State Energy Conversion Alliance (SECA) Core Technology Program by the U.S. Department of Energy's National Energy Technology Laboratory (NETL). Funding was additionally provided by the Boeing Fellowship.

References

[1] N. Bansal, E. Gamble, J. Power Sources 147 (2005) 107–115.
[2] S. Misture, A. Varshineya, M. Hall, S. Decarr, S. Bancheri, Glass and Glass-derivative Seals for Use in Energy-efficient Fuel Cells and Lamps, 2005, http://www.osti.gov/energycitations/servlets/purl/887322-NxOuqu/.
[3] J. Fergus, J. Power Sources 147 (2005) 46–57.
[4] N. Bansal, S. Choi, Ceram. Eng. Sci. Proc. 26 (2005) 275–283.
[5] K. Weil, J. Deibler, J. Hardy, D. Kim, G. Xia, L. Chick, C. Coyle, J. Mater. Eng. Perform. 13 (2004) 316–326.
[6] E. Stephens, J. Vetrano, B. Koeppel, Y. Chou, X. Sun, M. Khaleel, J. Power Sources 193 (2009) 625–631.
[7] H. Garmestani, D. Li, M. Khaleel, Mater. Sci. Forum 561–565 (2007) 315–318.
[8] S. Lin, H. Garmestani, Compos. Part B: Eng. 31 (2000) 39–46.
[9] H. Garmestani, S. Lin, B. Adams, Int. J. Plast. 14 (1998) 719–731.
[10] H. Garmestani, S. Lin, B. Adams, S. Ahzi, J. Mech. Phys. Solids 49 (2001) 589–607.
[11] D. Li, G. Saheli, M. Khaleel, H. Garmestani, CMC-Comput. Mater. Con. 4 (2006) 31–42.
[12] D. Li, G. Saheli, M. Khaleel, H. Garmestani, Comput. Mater. Sci. 38 (2006) 45–50.
[13] S. Lin, H. Garmestani, B. Adams, Int. J. Solids Struct. 37 (2000) 423–434.
[14] M. Hyatt, N. Bansal, J. Mater. Sci. 31 (1996) 172–184.
[15] N. Bansal, M. Hyatt, J. Mater. Res. 4 (1989) 1257–1265.
[16] S. Choi, N. Bansal, Ceram. Int. 31 (2005) 39–46.
[17] K. Weil, B. Koeppel, Int. J. Hydrogen Energy 33 (2008) 3976–3990.
[18] J. Milhans, S. Ahzi, H. Garmestani, M. Khaleel, X. Sun, B. Koeppel, Mater. Des. 30 (2009) 1667–1673.
[19] W. Liu, X. Sun, M. Khaleel, J. Power Sources 185 (2008) 1193–1200.
[20] G. Saheli, H. Garmestani, B. Adams, J. Comput. Aided Mater. Des. 11 (2004) 103–115.
[21] G. Saheli, H. Garmestani, A. Gokhale, in: S. Ghosh, J.K. Lee, J. Castro (Eds.), Proceedings of 8th International Conference on Numerical Methods in Industrial Forming Processes, American Institute of Physics, Melville, NY, 2004, pp. 355–359.
[22] J.M. Yang, L.T. Zhang, W.C. Zhou, in: A. Poursartip, K. Street (Eds.), Tenth International Conference on Composite Materials IV. Characterization and Ceramic Matrix Composites, Woodhead Publishing Limited, Cambridge, England, 1995, pp. 593–599.
[23] P. Corson, J. Appl. Phys. 45 (1974) 3159–3164.
[24] P. Corson, J. Appl. Phys. 45 (1974) 3165–3170.
[25] P. Corson, J. Appl. Phys. 45 (1974) 3171–3179.
[26] P. Corson, J. Appl. Phys. 45 (1974) 3180–3182.
[27] B. Adams, G. Canova, A. Molinari, Textures Microstruct. 11 (1989) 57–71.
[28] W. Voigt, Lehrbuch der Kristallphysik: Teubner (1928) 962.
[29] A. Reuss, Zeitschrift für Angewandte Mathematik und Mechanik 9 (1929) 49–58.
[30] S. Spinner, J. Am. Ceram. Soc. 39 (1956) 113–118.
[31] B. Beake, J. Smith, Philos. Mag. A 82 (2002) 2179–2186.
[32] P. Vullo, M. Davis, J. Non-Cryst. Solids 349 (2004) 180–184.
[33] H.H.K. Xu, T.A. Martin, J.M. Antonucci, F.C. Eichmiller, J. Dent. Res. 78 (1999) 706–712.